Results in Engineering 23 (2024) 102588

Contents lists available at ScienceDirect

Results in Engineering

journal homepage: www.sciencedirect.com/journal/results-in-engineering

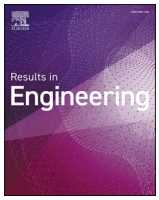

Case report

Design of a stirred batch reactor with scale-up to ensure efficient degumming process at a larger scale

Aditya Kurniawan [a], Syailendra Supit [b], Fatimah Azizah Riyadi [b,c], Md Zahangir Alam [d], Yuswan Muharam [b,*]

[a] Department of Chemical Engineering, UPN "Veteran" Yogyakarta. Sleman, Daerah Istimewa Yogyakarta, 55283, Indonesia
[b] Department of Chemical Engineering, University of Indonesia, Depok, Jawa Barat, 16424, Indonesia
[c] Research Center for Biomass Valorization, Universitas Indonesia, Depok, West Java, 16424, Indonesia
[d] Bioenvironmental Engineering Research Centre (BERC), Dept. of Biotechnology Engineering, Faculty of Engineering, International Islamic University Malaysia, Kuala Lumpur, 53100, Malaysia

ARTICLE INFO

Keywords:
Non-geometric scale-up
Computational fluid dynamics
Mass transfer coefficient
Degumming process
Stirred batch reactor

ABSTRACT

This study investigates the design of a stirred batch reactor with scale-up for the degumming of crude palm oil (CPO) using phosphoric acid (H_3PO_4). Laboratory-scale experiments were conducted in a triple-neck round vessel, followed by a scale-up to a larger-scale flat-bottom stirred tank reactor. Traditional scale-up methods using geometric similarity criteria are ineffective for reactors with different geometries; hence, this work introduces an improved approach using degumming efficiency, measured by gum concentration, as the similarity criterion to design the reactor. Computational Fluid Dynamics (CFD) was employed to model the velocity distribution and mass transfer processes, predicting gum concentration evolution through gum mass balances in the oil and aqueous phases. The simulation results showed that maintaining a minimum impeller speed of 93 rpm in the larger reactor effectively reproduced the best degumming efficiency observed in the laboratory reactor at 500 rpm and 60 °C. A strong correlation ($R^2 = 0.963$) was found between the modeled and empirical Sherwood numbers, indicating successful scale-up. This research demonstrates that degumming efficiency in a laboratory triple-neck round vessel can be numerically reproduced in a larger flat-bottom stirred tank reactor, providing valuable insights into the hydrodynamic characteristics unique to each geometry and marking a pivotal step in reactor scale-up methodologies.

1. Introduction

A process analysis to obtain optimum operating parameters is usually carried out in laboratory reactors. However, extrapolating the results to larger reactors is risky because correlations based on laboratory scale measurements lack local information and cannot be used to predict the homogeneity degree at specific locations [1,2]. The mixing process must be properly designed to avoid excessive energy input and undesirable products, especially in complex mixing problems [3]. Therefore, a scale-up method is necessary to adjust the operating conditions of a larger reactor to overcome this issue.

Current scale-up practices, which maintain a constant factor of ND^x require geometric similarity as the reactor size increases [3]. In many cases, this requirement cannot be applied due to specific technical specifications. Scale-up followed by corrections for geometric differences has been proposed to address this problem [4,5], but this approach is difficult to implement when significant geometrical differences exist.

The design of a stirred batch reactor with scale-up, particularly for liquid-liquid systems, relies on empirical correlations, best practices, and rules of thumb. The local variations of the hydrodynamic parameters obtained from such an approach do not align with real cases where the values vary significantly. Imperfect mixing plays a significant role in reactor performance, as demonstrated using the residence time distribution concept [6]. This approach divides a reactor into zones based on individual 'well-mixed' reactors [7,8]. However, residence time distribution data are specific and scale-limited, requiring a large number of experiments to acquire.

Computational fluid dynamics (CFD) has been widely used in the modelling, design, and scale-up of various reactors and processes

* Corresponding author.
E-mail address: muharam@che.ui.ac.id (Y. Muharam).

https://doi.org/10.1016/j.rineng.2024.102588
Received 1 June 2024; Received in revised form 14 July 2024; Accepted 17 July 2024
Available online 19 July 2024

[9–12]. Starting with simple single-phase models [13] (or assumed single-phase stirred tank reactors [14]), scale-ups using CFD have been undertaken. More sophisticated models of multiphase flow with individual momentum equation sets for each phase have been developed. In gas-liquid systems, Eulerian-Eulerian models have been utilized to analyze interphase mass transfer to supplement film theory-based correlations inside various types of reactors [15–19]. These models have also been incorporated into scale-up procedures [20–24]. For liquid-liquid systems, CFD has been used to model mixing and mass transfer in a reactor [25,26], all of which are still constrained by geometric similarities.

Significant computational resources are required to use a set of momentum equations for each phase (full multiphase models) [27]; therefore, a simpler multiphase model, i.e., mixture model, has been used as a substitute for reactor modelling and design [28,29]. In mixture models, continuity equations are solved for each phase, while momentum equations are solved for the mixture of continuous and dispersed phases clustering and large slip velocities occur, the application of this model becomes invalid [27]. These conditions usually arise during mixing with a large volume fraction of the dispersed phase.

The stirred tank reactor design with the aforementioned CFD-based scale-up still maintain geometric similarity. In most practical cases, laboratory-scale experiments are carried out in triple-neck round vessels where the fluids are stirred by a magnetic stirrer. Meanwhile, larger scale reactors are cylindrical tanks with flat or dish bottoms. Geometric similarities are no longer valid, rendering the design problem more complicated. Dimensions such as reactor diameter, impeller diameter, and fluid height are no longer linear and cannot be changed using the same factor.

Scale-up studies that do not adhere to the geometric similarity criterion are limited. An experimental analysis using a hot-wire velocity meter probe was carried out on the non-geometric scale-up of a fermenter [30]. It was still limited to following a certain ratio of the impeller diameter and reactor diameter to achieve adequate mixing. A study on the drop size distribution of a non-geometric liquid-liquid scale-up was also performed [31]. The flow was modeled using a one-dimensional plug-flow model, focusing on the breakup-coalescence phenomenon. The turbulent dissipation rate and circulation time were used as similarity criteria.

Hydrodynamic parameters (e.g., the Reynolds number, liquid mixing and circulation time, and impeller tip velocity) can be used as the similarity criterion in the scale-up of stirred tank reactors with different geometries in homogeneous systems [32]. If the process in the reactor is mass-transfer limited, the volumetric mass transfer coefficient is a well-known similarity criterion in fluid-fluid systems. Most applications of this criterion depend on the power per unit volume, discarding the space-dependent nature of the mass transfer. In multiphase reactor problems, mass transfer in the boundary layer sometimes is not the only rate-limiting step. Degumming efficiency can be used as a similarity criterion, such as the species concentration evolution for dynamic systems or reactant conversion profiles. CFD as a tool to characterize local hydrodynamics, can be used to scale up using these similarity criteria.

Degumming is a process of removing impurities such as phosphatides, metals, proteins, carbohydrates, and resins from crude palm oil (CPO). Iron, as one such content, was found to be responsible for unwanted flavor [33]. It exists as metal-phosphatide complexes, which require chemical treatment to be effectively removed from the oil. Phosphoric acid, being a stronger acid than phosphatidic acid [34], is utilized to decompose these complexes according to the reaction in Equation 1 [33]. The presence of water causes the precipitation of phosphatides, along with the acid, ions, and other sugar-like compounds previously bonded to the oil, to be separated via mechanical means [35]. This method is known as acid degumming, one of several degumming processes, which includes water degumming, dry degumming, enzymatic degumming, and membrane degumming [36,37].

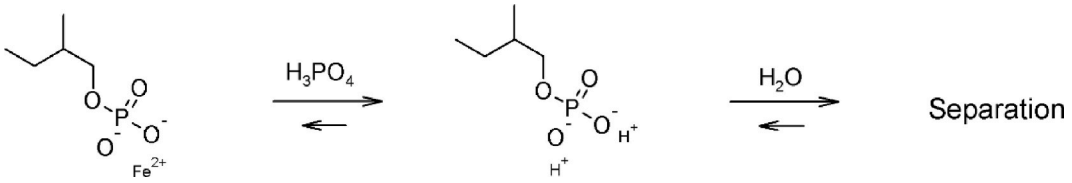

The transport of impurities between the immiscible oil and water (phosphoric acid) phases can be explained using the two-film theory. A boundary layer forms at the interface of the two phases. For the reaction to occur, the gum molecules need to cross the boundary layer into the water phase.

This paper presents the application of CFD in the design of a stirred batch reactor for the acid degumming process of crude palm oil (CPO) using phosphoric acid (H_3PO_4), with the evolution of gum concentration as the similarity criterion. The laboratory experiments were carried out in a triple-neck round flask. These experiments were then scaled up to obtain a larger scale reactor in the form of a flat-bottom stirred tank.

2. Materials and methods

The degumming experiments were carried out in a triple-neck round vessel filled with 100 ml of the mixture, consisting of CPO as the continuous phase and concentrated phosphoric acid solution (H_3PO_4 85 %) as the dispersed phase [37]. The laboratory reactor is a 1000 ml triple-neck round vessel with the specification listed in Table 1. A flat bottom tank of 1.250 m^3 liquid volume was specified as the larger scale reactor in this research with the specification being also listed in Table 1. The initial content of gum in the CPO was 1.43 % w/w and the initial volume fraction of the dispersed phase was 0.015. Agitation was

Table 1
Sizing data for laboratory and larger scale reactors.

Reactor	Data	Symbol	Value	
Laboratory reactor	Flask diameter	D_r	0.124	m
	Liquid volume	V_f	1.015×10^{-4}	m^3
	Liquid height	H_f	0.025	m
	Liquid surface diameter	D_f	0.099	m
	Stirrer bar length	L_{bar}	0.030	m
	Stirrer bar diameter	D_{bar}	0.006	m
Tank data				
Larger scale reactor	Liquid volume	V_f	1.250	m^3
	Liquid height	H_f	1.298	m
	Diameter	D_r	1.124	m
Impeller data				
	Number of blades	N_b	6	
	Diameter	D_{imp}	0.375	m
	Blade width	W_{imp}	0.075	m
	Blade length	L_{imp}	0.094	m
	Hub radius	R_{hub}	0.234	m
	Shaft diameter	D_{shaft}	0.038	m
	Baffle width	W_{baffle}	0.094	m

promoted by a magnetic stirrer, and the reaction was run for 120 minutes. Oil samples were withdrawn from the reactor to be analyzed for gum content every 15 minutes. Experiments were carried out for the impeller speed of 200 rpm–500 rpm at 60 °C, and the reactor temperature of 50 °C–80 °C at 350 rpm.

The momentum and mass transfer equations were numerically simulated to reproduce the 120-min evolution of the experimental gum concentrations. This was achieved by adjusting the values of the mass transfer coefficient k_c, the solubility coefficient K_{eq}, and the reaction rate coefficient k_{rx}. The model assumes that the gum concentration evolution was in a comparatively large time scale to the fluid flow. Thus, quantities obtained from the steady-state momentum equations were used for the unsteady-state mass transfer equations. Since a three-dimensional model was used, the calculated spatial concentrations need to be volume averaged to suit the experimental results.

At the same temperature, stirring for the different speeds of the impeller influences the mass transfer coefficient, while the reaction coefficient and the solubility constant remain the same. Temperature variation was intended to obtain the reaction rate coefficient the solubility constant. One of the time-dependent curves of the gum concentration from the laboratory experiments was chosen as the similarity criterion. The chosen curve is the one with the highest degumming efficiency within the experimental range. The larger scale reactor of the degumming process was expected to reproduce this time-dependent curve.

The mass transfer coefficient was then transformed into the Sherwood number according to Equation (2)

$$Sh_d = \frac{k_c d_d}{D_{AB}} \tag{2}$$

In order to determine the mass transfer coefficient in the larger reactor, an empirical Sherwood correlation for typical stirred tanks according to Equation (3) was introduced. The correlation is the simplest form of $Sh = f(Re_d, Sc)$, derived based on the boundary layer theory [38]. This form is also similar to the Garner and Keey [39] and Lochiel and Calderbank [40] correlation, where the natural convection term is absent.

$$Sh_d = c_1 Re_d^{c_2} Sc^{c_3} \tag{3}$$

The drop Reynolds number is defined as

$$Re_d = \frac{\rho_c |\mathbf{u}_{dc}| d_d}{\mu_c} \tag{4}$$

and the Schmidt number as

$$Sc = \frac{\mu_c}{\rho_c D_{AB}} \tag{5}$$

The drop diameter (d_d) and drop relative velocity ($\mathbf{u}_{dc}$) were derived

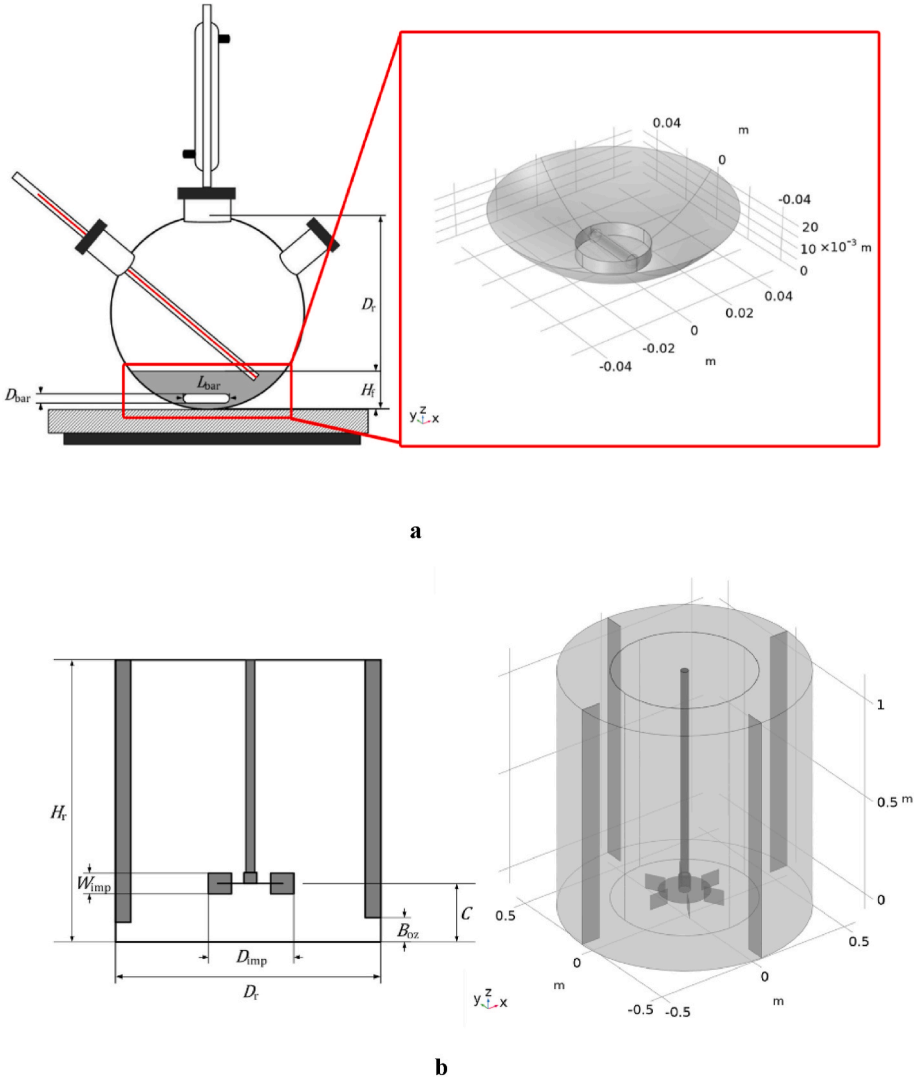

Fig. 1. Schematics and geometrical modelling of the laboratory (a) and larger-scale (b) reactor. The symbols used in the schematics are summarized in Table 1.

from the space-dependent variables of the CFD model. Equation (3) depends only on physical properties and hydrodynamic parameters for the range of the drop Reynolds number and the Schmidt number given by the laboratory reactor. Therefore it was used to describe mass transfer in the larger scale reactor.

The properties of each component used in the simulation were calculated using empirical equations available in the literature [41–44]. Variations of fluid volume in the reactors due to changes in fluid chemical composition and physical properties were neglected.

Constants in Equation (3) were determined through fitting of Equation (3) to Equation (2). Since the mass transfer coefficient, the interfacial area, the drop diameter, and the drop relative velocity calculated from the CFD model are the space-dependent quantities, their values in Equation (2) and Equation (3) were volume-averaged.

In the larger scale reactor model, the mass transfer coefficient was calculated using Equation (3) embedded to the mass transfer equation. The CFD and the mass transfer equations of the larger reactor were then solved numerically to obtain a time-dependent curve of the gum concentration that fits to the chosen time-dependent curve of the gum concentration of the laboratory reactor. This was achieved by adjusting the impeller speed.

3. Modelling and simulation

Since only 100 ml of fluid fill the 1000 ml triple-neck round vessel, the vessel was modeled as a portion of a sphere cut off by a plane, as illustrated in Fig. 1a. The portion of the sphere was divided into rotating and static domains. The rotating domain contains the rotating magnetic stirrer and the vicinity fluid. The static domain contains the rest fluid. For the larger scale reactor, the standard configuration was applied, i.e., a flat-bottom tank with baffles on all four sides of the tank wall (Fig. 1b). The liquid volume was divided into static and rotating domains. The rotating domain consists of a Rushton-type impeller with six blades and the vicinity fluid. The static domain contains the rest fluid. Rotating parts of the reactors were revolving in counterclockwise manner.

4. Mathematical modelling

To model the rotating fluid motion inside the reactor, the multiple reference frames (MRF) equation was applied. Coriolis and centrifugal forces were introduced as additional forces to the momentum equation. The simulation was run in the stationary mode (frozen rotor) to characterize mixing at steady state.

The effects of lift, virtual mass, Basset history, and turbulent dispersion forces were negligible compared to the drag force, and thus, were not considered in this study [45–47]. The dispersed phase was also regarded as a number of small drops dispersed throughout the vessel by the velocity field. On that account, interactions between drops (e.g., breakup-coalescence) were negligible. An algebraic slip velocity expression can be achieved by assuming the drops were accelerated instantaneously to their terminal velocity. These assumptions enabled the use of a scalar relation as a substitute for an individual momentum balance (Equation (7)), where acceleration of the drops was only influenced by gravity and/or centrifugal force. This allows the velocities of each phase to be solved using the mixture momentum balance. The mixture velocity is an averaged velocity of the dispersed and continuous phase.

$$\mathbf{u} = \left(1 - \frac{\phi_d \rho_d}{\rho}\right)\mathbf{u}_c + \frac{\phi_d \rho_d}{\rho}\mathbf{u}_d \tag{6}$$

$$\mathbf{u}_{dc} = \mathbf{u}_d - \mathbf{u}_c = \mathbf{u}_{slip} - \frac{\rho D_{md}}{\rho - \phi_d \rho_d}\frac{\nabla \phi_d}{\phi_d} \tag{7}$$

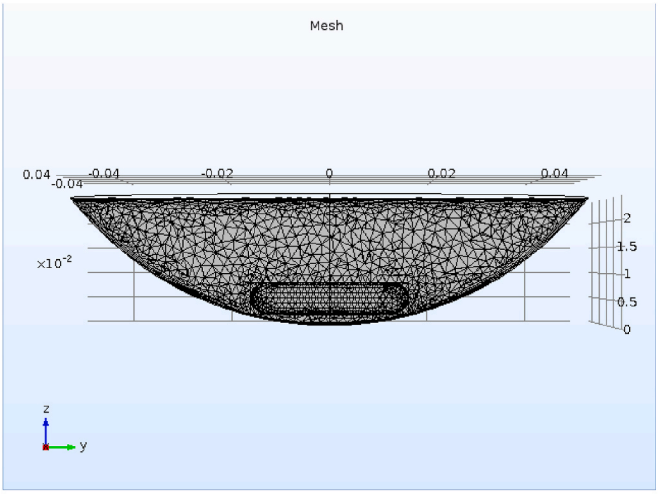

a

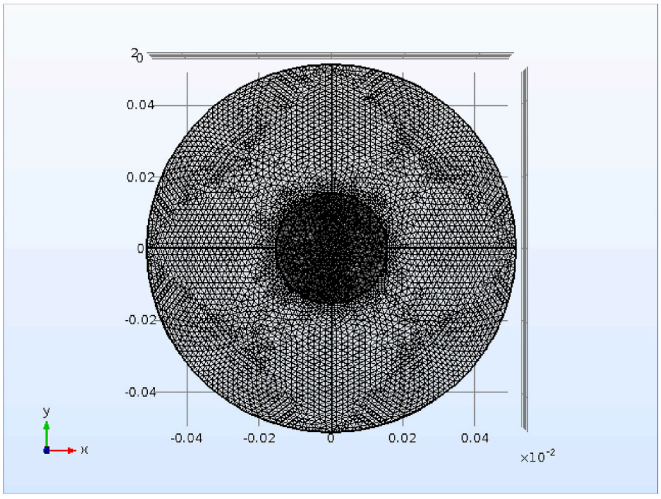

b

Fig. 2. Meshing for laboratory-scale reactor (a) vertical section (b) horizontal section.

The relative velocity also accounted for fluctuations due to the path dispersion phenomenon, driven by the concentration difference of drops. Continuity on each phase is preserved and the sum of the two individual continuity equation yields Equation (8). The momentum equation is solved as a mixture written in the form of Equation (9).

$$(\rho_c - \rho_d)\left(\nabla \cdot \left[\phi_d(1 - c_d)\mathbf{u}_{slip} - D_{md}\nabla \phi_d\right]\right) + \rho_c \nabla \cdot \mathbf{u} = 0 \tag{8}$$

$$\rho(\mathbf{u} \cdot \nabla)\mathbf{u} = \nabla \cdot \left[-p\mathbf{I} + (\mu + \mu_T)\left(\nabla \mathbf{u} + (\nabla \mathbf{u})^T - \frac{2}{3}(\nabla \cdot \mathbf{u})\mathbf{I}\right) - \frac{2}{3}\rho k\mathbf{I}\right] - \nabla \cdot \left[\rho c_d(1 - c_d)\left(\mathbf{u}_{slip} - \frac{D_{md}}{1 - c_d}\frac{\nabla \phi_d}{\phi_d}\right)\left(\mathbf{u}_{slip} - \frac{D_{md}}{1 - c_d}\frac{\nabla \phi_d}{\phi_d}\right)^T\right] + \rho \mathbf{g} + \mathbf{F} \tag{9}$$

At the boundary,

$$\mathbf{u} = 0$$

At the symmetry plane,

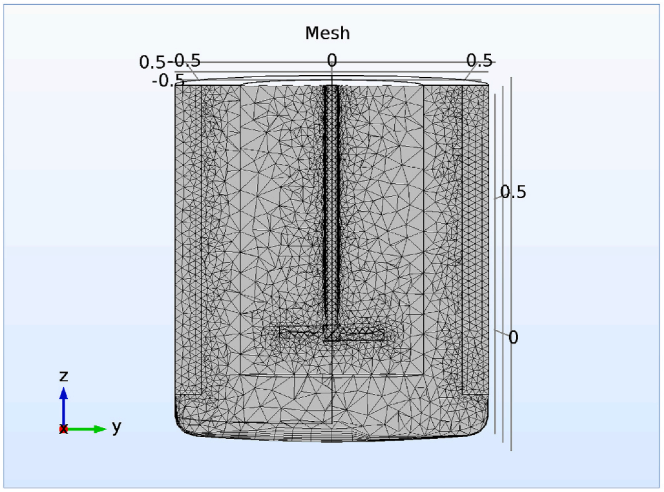

a

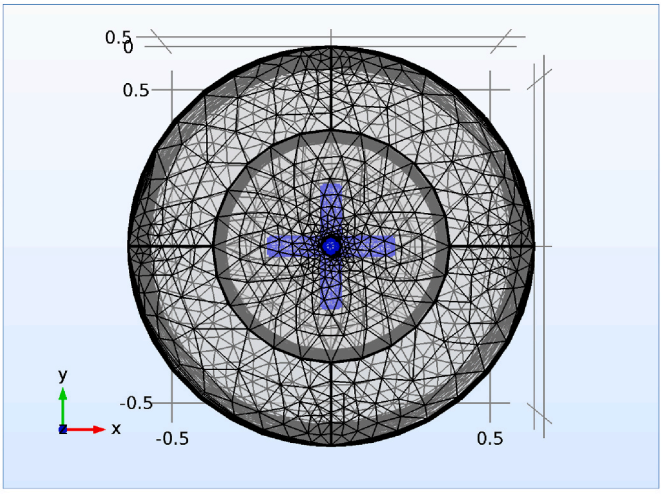

b

Fig. 3. Meshing for large-scale reactor (a) vertical section (b) horizontal section.

Table 2
Grid distributions of the laboratory and larger scale reactors.

Grid	Number of Elements
Laboratory reactor	
1	73,629
2	152,436
3	369,183
Larger scale reactor	
1	62,847
2	138,112
3	328,227

$$\frac{\partial \mathbf{u}}{\partial n}=0,\frac{\partial \mathbf{u}_{slip}}{\partial n}=0$$

Assuming viscous forces are still greater than or equal to the inertial forces, the Hadamard-Rybczynski drag model provided in Equation (10) was used to model the slip velocity [48].

$$\frac{3}{4}\frac{C_D}{d_d}\rho_c\|\mathbf{u}_{slip}\|\mathbf{u}_{slip}=\frac{(\rho_d-\rho)}{\rho}\left(\mathbf{g}+\frac{\mathbf{F}}{\rho}-(\mathbf{u}\cdot\nabla)\mathbf{u}\right) \quad (10)$$

$$C_D=\frac{24}{Re_t}\left(\frac{1+\frac{2}{3}\frac{\mu_c}{\mu_d}}{1+\frac{\mu_c}{\mu_d}}\right) \quad (11)$$

$$Re_t=\frac{\rho\|\mathbf{u}_{slip}\|d_d}{\mu} \quad (12)$$

Turbulence models are used to accommodate the instability in the fluid flow generated by the stirrer bar/impeller rotation. Reynolds-averaging is an acceptable approximation via the evaluation of numerical problems to the accuracy of the standard k-ε model [49]. Accordingly, Reynolds averaging of the convection-diffusion equations was applied in this study. Turbulence was manifested as additional stress in the momentum equation, which is calculated by solving two transport equations: turbulence kinetic energy and turbulence dissipation rate.

$$\rho\frac{\partial k}{\partial t}+\rho\mathbf{u}\cdot\nabla k=\nabla\cdot\left[\left(\mu+\frac{\mu_T}{\sigma_k}\right)\nabla k\right]+P_k-\rho\varepsilon \quad (13)$$

$$\rho\frac{\partial \varepsilon}{\partial t}+\rho\mathbf{u}\cdot\nabla\varepsilon=\nabla\cdot\left[\left(\mu+\frac{\mu_T}{\sigma_\varepsilon}\right)\nabla\varepsilon\right]+C_{\varepsilon1}\frac{\varepsilon}{k}P_k-C_{\varepsilon2}\rho\frac{\varepsilon^2}{k} \quad (14)$$

At the boundary,

$$k=0$$

$$\varepsilon=\varepsilon_{wall}$$

At the symmetry plane,

$$\frac{\partial k}{\partial n}=0,\frac{\partial \varepsilon}{\partial n}=0$$

The number of dispersed-phase drops was considered to be in diluted concentration, and therefore, was kept constant throughout the mixing process. The diameter and the specific interfacial area were calculated using the following expressions:

$$d_d=\left(\frac{6}{\pi}\frac{\phi_d}{n_d}\right)^{1/3} \quad (15)$$

$$a=\frac{(4\pi n_d)^{1/3}(3\phi_d)^{2/3}}{1-\phi_d} \quad (16)$$

To evaluate Equations (15) and (16), the transport equations for the dispersed-phase volume fraction (ϕ_d) and the drop number density (n_d) need to be solved. The transport of two quantities is governed by the velocity of the dispersed phase derived from Equation (6) to Equation (10). After several algebraic modifications, the two transport equations are expressed as follows:

$$\nabla\cdot\left[\phi_d\left(\mathbf{u}+(1-c_d)\mathbf{u}_{slip}-D_{md}\frac{\nabla\phi_d}{\phi_d}\right)\right]=0 \quad (17)$$

$$\nabla\cdot\left[n_d\left(\mathbf{u}+(1-c_d)\mathbf{u}_{slip}-D_{md}\frac{\nabla\phi_d}{\phi_d}\right)\right]=0 \quad (18)$$

At the boundary,

$$\mathbf{u}=0$$

At the symmetry plane,

$$\frac{\partial \phi_d}{\partial n}=0,\frac{\partial n_d}{\partial n}=0$$

The Neumann 'do-nothing' boundary condition was applied to the fluxes of velocity on both phases, number density, and dispersed volume fraction to depict the absence of transport beyond the wall. Conditions near the wall are influenced by the boundary layer phenomenon. Wall functions of the k-ε turbulence model were calculated analytically (logarithmic law) prior to the wall lift-off distance so that its meshing

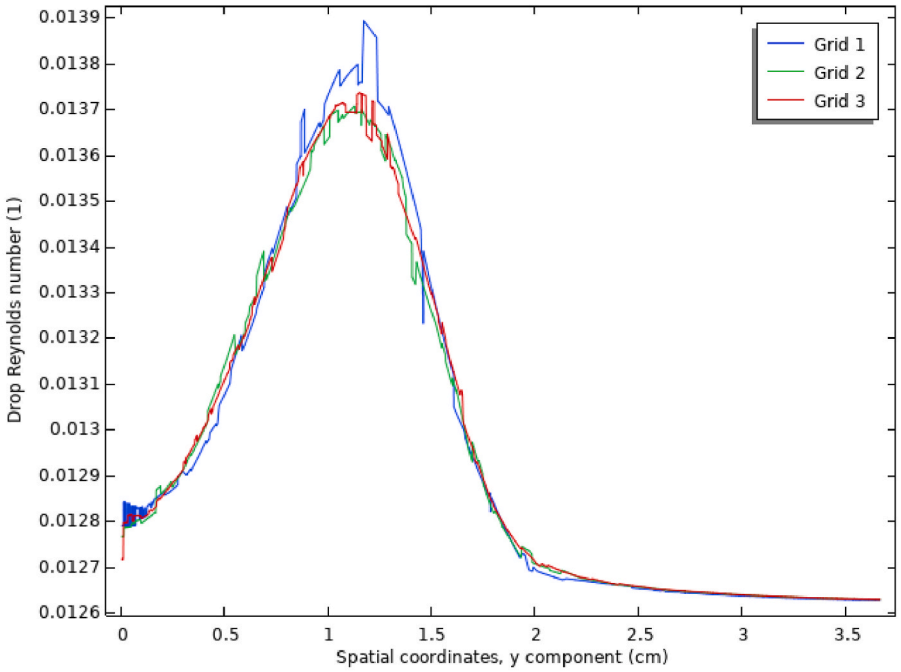

a

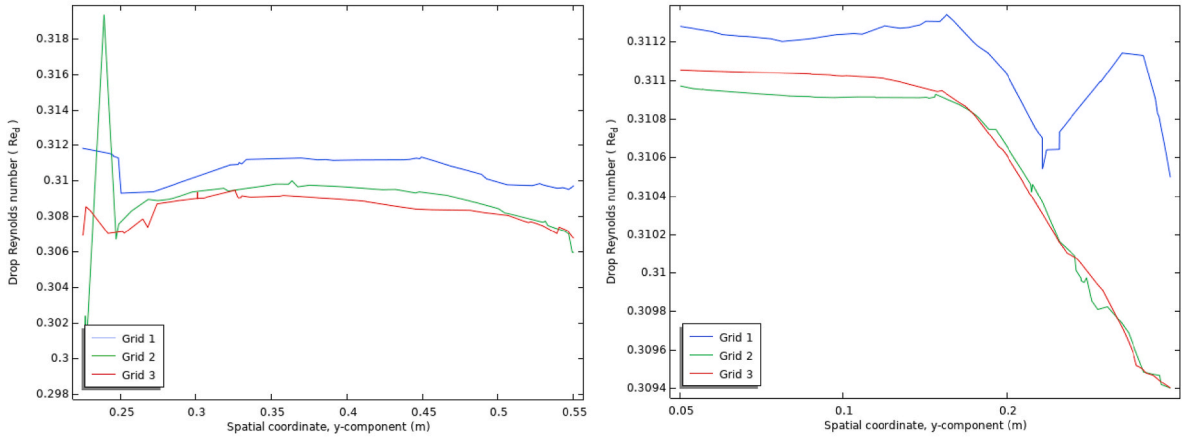

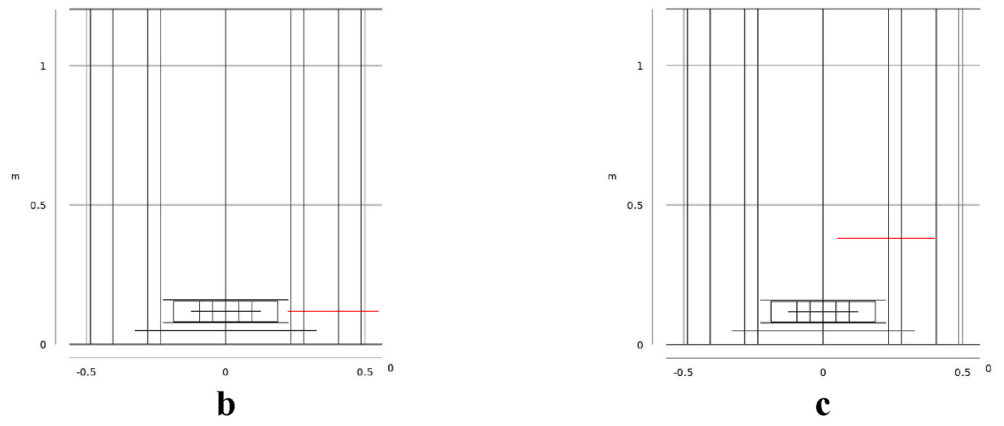

b **c**

Fig. 4. Grid dependence of the drop Reynolds number in the laboratory reactor (a) and larger scale reactor (b and c).

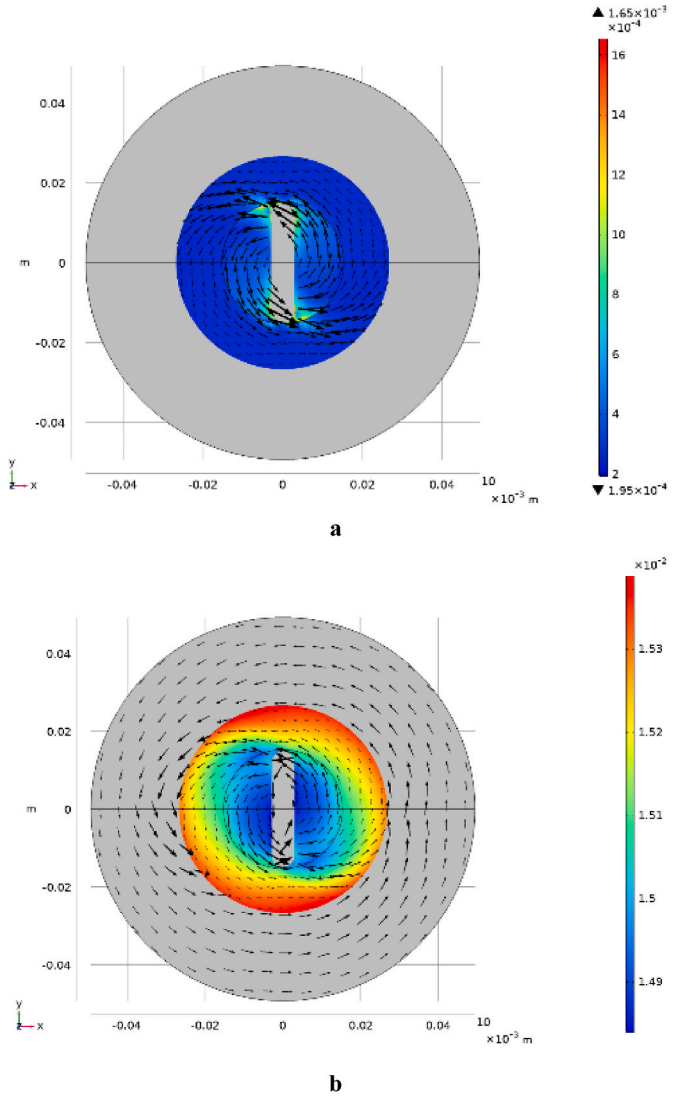

Fig. 5. Flow pattern with drop Reynolds number (a) and volume fraction (b) distribution of the laboratory-scale reactor at 500 rpm and 60 °C. Higher value are represented with increasing color wavelength. The arrows represent the flow pattern in three dimensions. (For interpretation of the references to color in this figure legend, the reader is referred to the Web version of this article.)

grid can be stretched. The viscos and turbulent stresses of this area are a function of the tangential velocity. The turbulent kinetic energy does not change in areas near the wall, and the turbulent dissipation rate is calculated using the von Karman wall function. The interior wall boundary condition was applied on the boundary between the internal parts, which have infinitesimal thickness in order to reduce the grid density. This internal wall boundary equation is identical to the normal wall, with additional upwind and downwind terms to accommodate discontinuity of the infinitesimal thickness. The condition applied to the impellers is the rotating wall boundary condition, which comprises of the same wall functions but with the relative velocity as the rotating domain velocity.

The degumming reaction was considered as irreversible and second order in relation to the gum and phosphoric acid concentrations. Two mass balances representing gum transport from the oil phase to the aqueous phase and one phosphate balance were constructed accordingly. The boundary layer mass transfer and reaction rates were incorporated in the equations as the consumption/production term. Concentrations was assumed in a comparatively large time scale to the fluid flow, where the flow should have achieved steady-state early in the

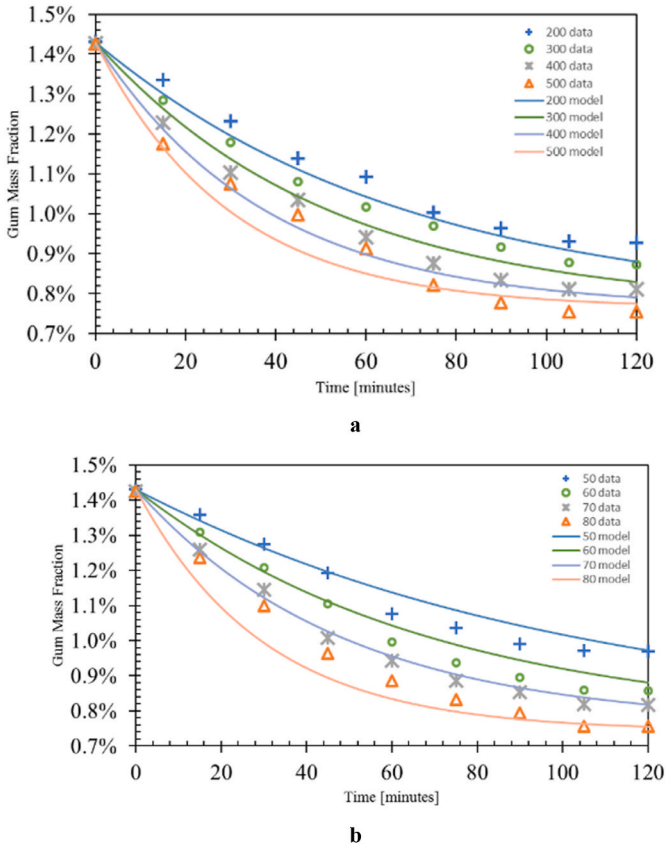

Fig. 6. Gum concentration of experiments (symbols) and simulations (lines) at the impeller speed (a) and temperature (b) variation.

Table 3
Results of concentration fitting.

Speed [rpm]	Temperature [°C]	k_c [10^9 m/s]	k_{rx} [10^3 ml/(g.min)]	K_{eq}
200	60	4.529	0.0041	54.98
300	60	3.369	0.0041	54.98
400	60	3.092	0.0041	54.98
500	60	2.908	0.0041	54.98
350	50	1.282	0.0027	54.88
350	60	2.031	0.0041	54.98
350	70	2.995	0.0061	55.35
350	80	5.066	0.0092	58.31

evolution. Thus, variables obtained from the steady-state momentum equations were used for this time dependent study.

The mass balances of gum in the oil phase and the aqueous phase are described by Equation (19) and Equation (20). The mass balance of phosphate in the aqueous phase is described by Equation (21). In each mass balance, the distribution of gum and phosphate molecules in each bulk fluid occurs by convection.

$$\frac{\partial c_{gum}^{(o)}}{\partial t} + (\mathbf{u}_c \cdot \nabla) c_{gum}^{(o)} = -k_c a \left(K_{eq} c_{gum}^{(o)} - c_{gum}^{(w)} \right) \tag{19}$$

$$\frac{\partial c_{gum}^{(w)}}{\partial t} + (\mathbf{u}_d \cdot \nabla) c_{gum}^{(w)} = k_c a \left(K_{eq} c_{gum}^{(o)} - c_{gum}^{(w)} \right) \left(\frac{1-\phi_d}{\phi_d} \right) - k_{rx} c_{gum}^{(w)} c_{ph} \tag{20}$$

$$\frac{\partial c_{ph}}{\partial t} + (\mathbf{u}_d \cdot \nabla) c_{ph} = -k_{rx} c_{gum}^{(w)} c_{ph} \tag{21}$$

$$k_{rx} = A \exp\left(\frac{-E_a}{RT} \right) \tag{22}$$

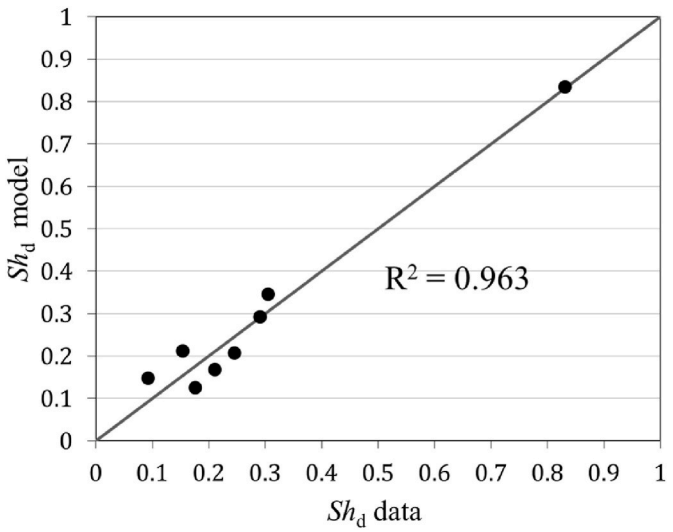

Fig. 7. Comparison between the Sherwood numbers data and the Sherwood numbers model.

At $t = 0$, $c_{gum}^{(o)} = 1.43$ % w/w of continuous phase, $c_{gum}^{(w)} = 0$, and $c_{ph} =$ 85 % of dispersed phase.

The model was solved using COMSOL Multiphysics. Momentum equations were available in the built-in Rotating-Machinery Mixture Model module. The dependent variables were solved in a segregated group for the velocity and pressure, turbulence variables, and volume fraction, each using the PARDISO solver. The local residual that measures the error at each point within the domain is used as an indicator of convergences. For the larger reactor, several simulations were run with different impeller speeds to achieve the target profile.

In this study, the grid size (meshing) was chosen based on the required calculation accuracy and the available RAM capacity. Adjustments to the meshing were made if the iteration results showed errors or failed to converge. For a laboratory-scale reactor, standard grid settings were used with grid sizes ranging from 1.97×10^{-4} m–0.0033 m. Meshing for the laboratory-scale reactor is shown in Fig. 2.

For a large-scale reactor, a User Controlled Grid was implemented, with grid sizes ranging from 0.0225 m to 0.146 m. Fig. 3 depicts the meshing for the large-scale reactor. Selecting the optimal grid size for a large-scale reactor is challenging due to its intricate geometry, which leads to complex flow patterns. An appropriate grid size is crucial for obtaining accurate and convergent simulation results.

5. Results and discussion

All governing equations were numerically solved and the calculated quantities were reported in color scales and streamlines.

5.1. Grid independence

The grid sensitivity study was performed on both reactors using three different sizes of 3-D grid. They consist of free tetrahedral sequence distributed using Delaunay tesselation. The different maximum and minimum sizes of elements were specified in the static and rotating domains, resulting in the total number of elements given in Table 2.

Fig. 4 shows the drop Reynolds number distribution along red horizontal lines in the laboratory and larger scale reactors. The drop Reynolds number was shown to be grid dependent up to about 152,436 domain elements in the laboratory reactor and 138,112 domain elements in the larger reactor. For the laboratory reactor, the relative error of the drop Reynolds numbers calculated with Grid 1 to those with Grid 2 (denser grid) were 0.16%–1.26 %, and calculated with Grid 2 to those with Grid 3 (denser grid) were 0.13%–1.17 %. For the larger scale reactor, the error of the drop Reynolds numbers calculated with Grid 1 relative to Grid 2 is 7.90%–8.47 %, and calculated with Grid 2 relative to Grid 3 is 4.52–4.82 %. A similar trend also occurred in the velocity magnitude and dispersed fraction. In order to save calculation time, Grid 2 was then used in simulations of the laboratory reactor and the larger reactor.

5.2. Laboratory reactor simulation

Fig. 5 shows the flow patterns in the laboratory reactor resulting from the simulations. The maximum velocity of the liquid mixture occurs near the stirrer bar tip, as indicated by the intensity of arrows in Fig. 5a. The increase in velocity in front of the stirrer bar tip indicates that the fluid body is accelerated by the impact with the stirrer bar, while the increase behind the stirrer bar tip occurs due to the void created by the rotating motion. This void is associated with a low-pressure zone so that the fluid flows into the void [50]. These trailing vortices promote dispersion of drops in areas behind the impeller tip, resulting in a sparser distribution of drops, as shown in Fig. 5b.

Although having a similar order to the drop Reynolds number, increased turbulence in front of the tip behaves differently. The dispersed phase is more concentrated on the tip of the impeller due to the momentum generated by the stirrer bar motion. The momentum is dissipated away from the rotation zone along with the turbulence intensity, therefore producing a lower order of turbulence in zones near the wall.

The flow pattern also indicates that solid body vortices are formed. These vortices revolve along the direction of the stirrer bar rotation. Around the tip of the impeller, smaller vortices were also observed due to the movement of the impeller. Unlike trailing vortices, solid body vortices do not promote dispersion since the dimension of these vortices are much larger. The dispersed phase only follows the flow pattern without dispersing effectively. Formation of these vortices can be mitigated by incorporating baffles inside the reactor [48]. A similar trend of velocity distribution, flow pattern, and turbulence intensity was perceived in other operating conditions, but with different magnitudes. This infers that hydrodynamic parameters from the simulation are more influenced by the geometrical configuration of the reactor.

Fig. 6 shows the 120-min evolution of the experimental and calculated gum concentrations. In the laboratory reactor. Fig. 6a is for the variation of the impeller speed at 60 °C, and Fig. 6b is for the variation in temperature at 350 rpm. The simulation curves are the best fitting results to the experimental ones at different impeller speeds and temperatures. During the fitting process, the mass transfer coefficient k_c, the solubility constant K_{eq}, and the reaction rate coefficient k_{rx} were adjusted. The values of those parameters providing the best fitting are depicted in Table 3. The data processing in the form of the relationship between the reaction rate coefficient and the temperature provides the values of the Arrhenius parameters. The values obtained are 4507.7 ml/(g·min) for the pre-exponential factor and 38.503 J/(mol·K) for the activation energy.

5.3. Correlation for mass transfer coefficient

Multilinear regression was applied to develop a correlation for the mass transfer coefficient according to Equation (3). The Sherwood number is the dependent variable in the correlation while the drop Reynolds number and the Schmidt number are the independent variables. A data set consisting of the values of temperature, impeller speed, and mass transfer coefficient as shown in Table 3 were used as the regression data. The resulted c_1, c_2, and c_3 are 0.0044, 0.573, and 0.464, respectively. Equation (3) is then written in the form of Equation (23). The coefficient of determination (R^2) giving these values is 0.963, which shows a strong correlation between the modeled Sherwood number and the empirical Sherwood number, as shown in Fig. 7. The exponent of the

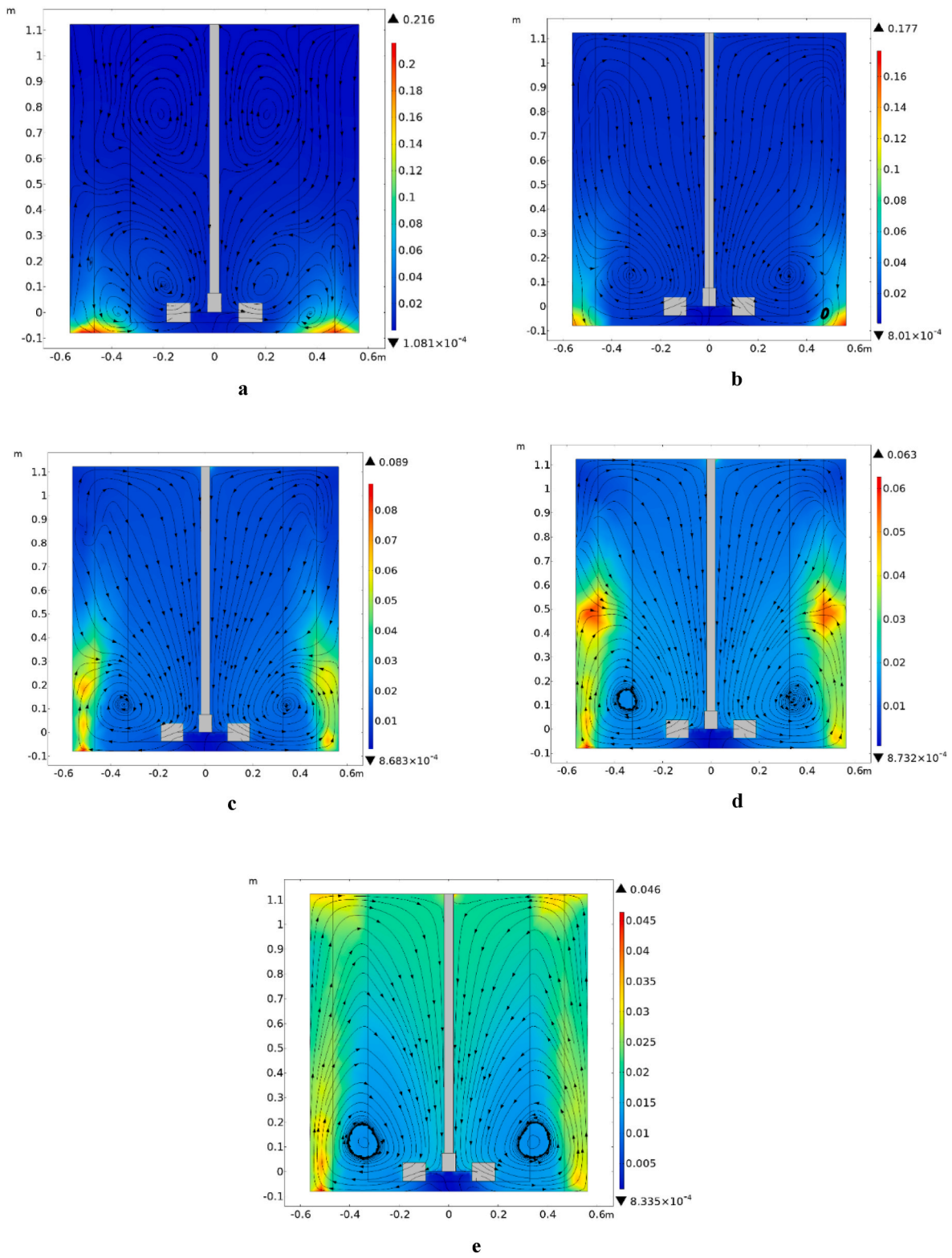

Fig. 8. Flow pattern and dispersed-phase volume fraction distribution for the larger reactor at 40 rpm (a), 75 rpm (b), 93 rpm (c), 141 rpm (d), and 500 rpm (e). Higher value are represented with increasing color wavelength. The streamlines represent the projected flow pattern in the yz-plane in the middle of the reactor. (For interpretation of the references to color in this figure legend, the reader is referred to the Web version of this article.)

drop Reynolds number is higher than that of the Schmidt number in Equation (23). This indicates that the Reynolds number has a stronger influence on the Sherwood number than the Schmidt number. Therefore, the mass transfer coefficient dependence on mixing intensity is higher than on temperature.

$$Sh_d = 0.0044\, Re_d^{0.573} Sc^{0.464} \tag{23}$$

As shown in Fig. 6a, the best degumming efficiency within the experimental range is at 500 rpm and 60 °C, at which the gum concentration has approached equilibrium at the end of the operation.

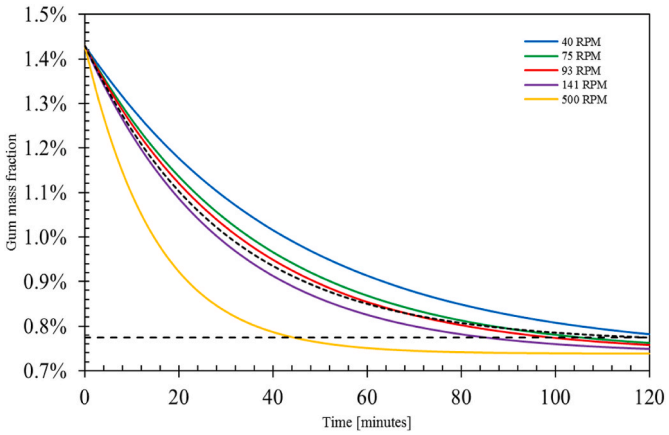

Fig. 9. Gum concentrations for various impeller speeds of the larger scale reactor.

Therefore, the curve at this condition was chosen as the similarity criterion.

5.4. Larger scale reactor simulation

As is the case in the laboratory reactor, the fluid flow was more intensive near the impeller, as indicated by the streamlines. The velocity profiles observed from the horizontal slice are also similar to the laboratory reactor with the same effect of trailing vortices along the six blades of the Rushton turbine.

A radial flow pattern was formed in the larger reactor by the action of the radial-type impeller (Fig. 8). Approaching the wall, the flow was diverted in the axial direction by the baffle. It was then fed back into the impeller region. This circulation pattern in the lowest impeller speed was more complex vertically as gravity plays a more significant role in the larger reactor. The pattern becomes more consistent along with the increase of impeller speed. It is caused by the decreasing influence of the graviational force to the droplets as it is shown by the Froude number. A minimum speed of 141 rpm is needed to fully overcome the influence of gravitational force.

The wall jet effect was discovered, especially on high impeller speed (500 rpm), where inertial forces surpassed gravitational forces by more than two-fold. The presence of baffles promotes vertical circulation inside the tank in the form of an internal annular jet [51]. Radial impellers cause significant momentum loss during collision with the wall. Consequently, combined with the immense effect of gravitational forces, the wall jet effect on lower impeller speeds was less pronounced.

The distribution of the dispersed-phase volume fraction in Fig. 8 represents the quality of dispersion inside the reactor. At a lower impeller speed (40 rpm), separation occurs, in which the dispersed phase is clustered at the bottom of the reactor, where around 9–20 % of the space was filled with the dispersed phase. This phenomenon is also caused by the dominance of the gravitational forces working on the heavier dispersed phase over the inertial force generated by impeller rotation. This trait is a consequence of the distinct geometry between the two reactors.

Coalescence may occur in the concentrated zones. Accommodation of interactions between drops should be considered in the model. A compartmentalization approach to preserve the computational resource, as done by Bashiri et al. [21] may be used to segregate these zones that require a more representative model.

At 75 rpm, the maximum local dispersed phase fraction drops to around 17 %. Leng and Calabrese [52] classified the dispersed fraction on the range of 1–20 % as moderately concentrated systems. Ideal dilute dispersion theories may still apply if this system of CPO and phosphoric acid can be described as a noncoalescing system.

It is inferred that there is a minimum impeller speed required to balance the gravitational force, thus improving the distribution of the dispersed phase. Skelland and Seksaria [53] developed a minimum Froude number correlation regarding this phenomenon on liquid-liquid mixing. According to this correlation, the minimum Froude number required for this geometry is 0.44, although this correlation was developed for dispersed phase concentration of around 50 %. Evidently, the accumulation starts to distribute more evenly at a lower Froude number of 0.092 (93 rpm).

On the gum concentration evolution, the gum concentrations have not reached equilibrium after 120 seconds except for 500 rpm as shown in Fig. 9. However, mechanical stability may be an issue at 500 rpm. The mass transfer coefficient becomes larger with increasing impeller speed because the averaged drop diameter becomes smaller at higher impeller speeds and creates a larger specific interfacial area. Moreover, turbulence becomes more prominent, thereby increasing its mass transfer coefficient. Due to the small amount of gum in the oil, the relatively high reaction rate coefficient, and the temperature being kept constant, the overall gum consumption is highly affected by mass transfer. Therefore, increasing the impeller speed results in faster gum consumption.

The curve with the evolution closest to the similarity criterion is the one in which the processs were stirred with the impeller rotation speed of 93 rpm and 141 rpm. This curve is the dotted black one in Fig. 9. Therefore, in order to reproduce the best degumming efficiency obtained in the laboratory reactor in the larger reactor or better, the impeller speed in the larger scale reactor should be the same as giving the dotted black curve or higher, provided the mechanical stability of rotation is maintained.

Nevertheless, the effect of disparity in flow pattern between the laboratory reactor and the larger scale reactor to the mass transfer needs to be investigated. This can be performed through validation, i.e., by comparing the simulation results with the experimental ones of the larger reactor proposed in this work. In addition, the impact of a more pronounced gravitational effect is required to be taken into account. This may affect the mechanism of mass transfer, where applicability of Equation (23) as an empirical correlation is a subject of further investigation. A semi-theoretical correlation for the mass transfer coefficient is a recommended approach since it depends directly on physical (diffusivity) and hydrodynamical (relative velocity or turbulent dissipation rate) properties.

6. Conclusions

In conclusion, the proposed systematic approach effectively designs a stirred batch reactor for degumming CPO. The use of CFD with the Mixture model and the k-ε turbulence model, along with mass balances, provides a reliable method for characterizing mass transfer in both laboratory and larger scale reactors. The larger flat-bottom stirred tank reactor successfully reproduces the gum concentration evolution observed in the laboratory triple-neck round vessel, achieving optimal efficiency at speeds between 93 rpm and 141 rpm. However, the significant hydrodynamic differences between the two reactor geometries, such as the gravity effect, should be carefully considered during the scale-up process to ensure accurate replication of results.

Symbols used

A	[m^3/(kg.s)]	pre-exponential factor
a	[m^{-1}]	specific interfacial area
B_{oz}	[m]	baffle clearance
C	[m]	impeller bottom clearance
$c_{gum}^{(o)}$	[kg/m^3]	gum concentration in the oil phase
$c_{gum}^{(w)}$	[kg/m^3]	gum concentration in the water phase
c_{ph}	[kg/m^3]	phosphate concentration
C_d	[−]	drag force coefficient

(continued on next page)

(*continued*)

C_μ	[−]	turbulence model constant
D_{AB}	[m^2/s]	diffusivity coefficient
E_a	[J/(mol.K)]	activation energy
D_{imp}	[m]	impeller diameter
D_{md}	[m^2/s]	turbulence dispersion coefficient
D_r	[m]	reactor diameter
d_d	[m]	drop diameter
F	[N/m^2]	total force flux
g	[m/s^2]	gravity acceleration
I	[−]	identity matrix
K_{eq}	[−]	solubility coefficient
k	[m^2/s^2]	turbulence kinetic energy
k_c	[m/s]	total mass transfer coefficient
$k_c a$	[1/s]	Volumetric mass transfer coefficient
k_{rx}	[m^3/(kg.s)]	reaction rate constant
N	[1/s]	impeller speed
n_d	[1/m^3]	drop number density
p	[Pa]	pressure
P_k	[W/m^3]	turbulent kinetic energy source term
Re_d	[−]	drop Reynolds number
Sc	[−]	Schmidt number
Sh_d	[−]	Sherwood number
T	[K]	reacting temperature
u	[m/s]	mixture velocity
$\mathbf{u}_c$	[m/s]	continuous phase velocity
$\mathbf{u}_d$	[m/s]	dispersed phase velocity
$\mathbf{u}_{dc}$	[m/s]	drop relative velocity
$\mathbf{u}_{slip}$	[m/s]	slip velocity
ε	[m^2/s^3]	turbulence dissipation rate
ϕ_d	[−]	dispersed-phase volume fraction
μ	[kg m/s]	mixture viscosity
μ_c	[kg m/s]	continuous phase viscosity
μ_d	[kg m/s]	dispersed phase viscosity
μ_T	[kg m/s]	turbulent viscosity
ρ	[kg/m^3]	mixture density
ρ_c	[kg/m^3]	continuous phase density
ρ_d	[kg/m^3]	dispersed phase density
σ_k	[N/m^2]	turbulence model constant
σ_ε	[N/m^2]	turbulence model constant
$\sigma_{\varepsilon 2}$	[N/m^2]	turbulence model constant

Statement of competing interests

The simulation was conducted in the Chemical Process Simulation Laboratory of the Department of Chemical Engineering, University of Indonesia using the Mixing and CFD Module of COMSOL® Multiphysics 5.2 under the academic license of Dr. Muharam. The authors declare no potential conflict of interest.

CRediT authorship contribution statement

Aditya Kurniawan: Software, Formal analysis, Data curation. **Syailendra Supit:** Writing – original draft, Investigation, Formal analysis, Data curation. **Fatimah Azizah Riyadi:** Writing – review & editing. **Md Zahangir Alam:** Formal analysis, Writing – review & editing. **Yuswan Muharam:** Writing – review & editing, Validation, Supervision, Software, Investigation, Funding acquisition, Conceptualization.

Declaration of competing interest

The authors declare that they have no known competing financial interests or personal relationships that could have appeared to influence the work reported in this paper.

Data availability

Data will be made available on request.

Acknowledgement

The research was supported by the program of Hibah Publikasi Terindeks Internasional (PUTI) Q1 2024–2025, grant number NKB-548/UN2.RST/HKP.05.00/2024, which was granted by the Universitas Indonesia in 2024.

References

[1] T. Post, Understand the real world of mixing, Chem. Eng. Prog. 106 (3) (2010) 25–32.
[2] M. Jahoda, M. Moštěk, A. Kukuková, V. Machoň, CFD modelling of liquid homogenization in stirred tanks with one and two impellers using large eddy simulation, Chem. Eng. Res. Des. 85 (5) (2007) 616–625.
[3] D.E. Leng, R.V. Calabrese, Immiscible liquid–liquid systems, in: E.L. Paul, V. A. Atiemo-Obeng, S.M. Kresta (Eds.), Handbook of Industrial Mixing, John Wiley & Sons, 2004, pp. 639–753.
[4] D.S. Dickey, Scale-up, in: P.J. Cullen, R.J. Romañach, N. Abatzoglou, C.D. Rielly (Eds.), Pharmaceutical Blending and Mixing, John Wiley & Sons, 2015, pp. 345–368.
[5] D.S. Dickey, Liquid agitation, in: T.G. Hicks, N. Chopey (Eds.), Handbook of Chemical Engineering Calculations, fourth ed., McGraw-Hill, 2012. Section 12.
[6] P. Danckwerts, Continuous flow systems: distribution of residence times, Chem. Eng. Sci. 2 (1953) 1–13.
[7] K. Kiared, F. Larachi, C. Guy, J. Chaouki, Trajectory length and residence-time distributions of the solids in three-phase fluidized beds, Chem. Eng. Sci. 52 (1997) 3931–3939.
[8] V. Ranade, Computational Flow Modeling for Chemical Reactor Engineering, Academic Press, 2001.
[9] Wen-Tao Yan, et al., The effect of aspect ratio on hydraulic and heat transfer characteristics in a fractal microchannel, Int. J. Fluid Mech. Res. 47 (2020) 1.
[10] Cong Li, et al., Thermohydraulic characteristics of microchannel heat sinks combined with ribs and cavities: effects of geometric parameters and heat flux, Heat Tran. Res. 50 (2019) 1.
[11] Wei-Biao Ye, et al., Study on thermal uniformity and improvement for the drying of lithium-ion batteries, Int. J. Fluid Mech. Res. 46 (2019) 6.
[12] Wei-Biao Ye, et al., Validation of thermal modeling of unsteady heat source generated in a rectangular lithium-ion power battery, Heat Tran. Res. 50 (2019) 3.
[13] V. Koganti, F. Carroll, R. Ferraina, R. Falk, Y. Waghmare, M. Berry, Gaudio. Application of modeling to scale-up dissolution in pharmaceutical manufacturing, AAPS PharmSciTech 11 (4) (2010) 1541–1548.
[14] R.Z. Davis, Design and Scale-Up of Production Scale Stirred Tank Fermenters, Utah State University, Thesis, 2010.
[15] W. Williams-Dalson, H. Zhang, E. Keshavarz-Moore, P.A. Shamlou, Computational fluid dynamics (CFD) analysis of mixing and gas-liquid mass transfer in shake flasks, Biotechnol. Appl. Biochem. 41 (2005) 1–8.
[16] J.D. Ramsey, M. Amer, Y. Feng, Using CFD simulations and statistical analysis to correlate oxygen mass transfer coefficient to both geometrical parameters and operating conditions in a stirred-tank bioreactor, Biotechnol. Prog. 35 (3) (2019) e2785.
[17] F. Kerdouss, A. Bannari, P. Proulx, R. Bannari, M. Skrga, Y. Labrecque, Two-phase mass transfer coefficient prediction in stirred vessel with a CFD model, Comput. Chem. Eng. 32 (2008), 1973-1955.
[18] W. Tang, A. Pan, H. Lu, J. Xia, Y. Zhuang, S. Zhang, Noorman, H. Improvement of glucoamylase production using axial impellers with low power consumption and homogeneous mass transfer, Biochem. Eng. J. 99 (2015) 167–176.
[19] D. Cheng, X. Feng, J. Cheng, C. Yang, Numerical simulation of macro-mixing in liquid-liquid stirred tanks, Chem. Eng. Sci. 101 (2013) 272–282.
[20] M. Li, G. White, D. Wilkinson, K.J. Roberts, Scale up study of retreat curve impeller stirred tanks using LDA measurements and CFD simulation, Chem. Eng. J. 108 (1–2) (2005) 81–90.
[21] H. Bashiri, F. Bertrand, J. Chaouki, Development of a multiscale model for the design and scale-up of gas/liquid stirred tank reactors, Chem. Eng. J. 297 (2016) 277–294.
[22] J. Gimbun, C.D. Rielly, Z.K. Nagy, Modelling of mass transfer in gas–liquid stirred tanks agitated by Rushton turbine and CD-6 impeller: a scale-up study, Chem. Eng. Res. Des. 87 (4) (2009) 437–451.
[23] J. Morchain, J. Gabelle, A. Cockx, A coupled population balance model and CFD approach for the simulation of mixing issues in lab-scale and industrial bioreactors, AIChE J. 60 (1) (2014) 27–40.
[24] L. Niño, M. Peñuela, G.R. Gelves, CFD prediction of gas-liquid mass transfer in a large-scale spin filter bioreactor, Int. J. Appl. Eng. Res. 11 (6) (2016) 4500–4507.
[25] S. Ibemere, S.M. Kresta, Modelling the mixing and dissolution kinetics of partially miscible liquids, Chem. Eng. Res. Des. 85 (A5) (2005) 710–720.
[26] L. Abu-Farah, F. Al-Qaessi, A. Schönbucher, Cyclohexane/water dispersion behaviour in a stirred batch vessel experimentally and with CFD simulation, Procedia Comput. Sci. 1 (1) (2010) 655–664.
[27] M. Manninen, V. Taivassalo, S. Kallio, On the Mixture for Multiphase Flow, 288, VTT Publications, 1996, pp. 1–67.
[28] L. Meng, J.-C. Cheng, H. Jiang, C. Yang, W.-H. Xing, W.-Q. Jin, Design and analysis of a submerged membrane reactor by CFD Simulation, Chem. Eng. Technol. 36 (11) (2013) 1874–1882.
[29] G. Venturini, M.B. Goldschmit, Gas-liquid reaction model in gas-stirred systems: Part 1. Numerical model, Metall. Mater. Trans. 38B (3) (2007) 461–475.
[30] J.Y. Oldshue, Fermentation mixing scale-up techniques, Biotechnol. Bioeng. 8 (1) (1996) 3–24.

[31] W. Podgórska, J. Bałdyga, Scale-up effects on the drop size distribution of liquid–liquid dispersions in agitated vessels, Chem. Eng. Sci. 56 (3) (2001) 741–746.
[32] G.D. Najafpour, Bioprocess scale-up, in: Biochemical Engineering and Biotechnology, Elsevier, 2015, pp. 287–381.
[33] A.J. Dijkstra, M. Van Opstal, The total degumming process, J. Am. Oil Chem. Soc. 66 (7) (1989) 1002–1009.
[34] A. Hvolby, Removal of nonhydratable phospholipids from soybean oil, J. Am. Oil Chem. Soc. 48 (9) (1971) 503–509.
[35] H.J. Ringers, J.C. Segers, United States of America Patent No. 4,049, 1977, p. 686.
[36] O. Zufarov, S. Schmidt, S. Sekretar, Degumming of rapeseed and sunflower oils, Acta Chim. Solv. 1 (2008) 321–328.
[37] Y. Ristianingsih, Sutijan, A. Budiman, Kinetic study of chemical and physical degumming of crude palm oil (CPO) using phosphoric acid, Reaktor 13 (4) (2011) 242–247.
[38] R. Ghotli, A. Abdul Aziz, S. Ibrahim, Liquid-liquid mass transfer studies in various stirred vessel designs, Rev. Chem. Eng. 31 (4) (2015) 329–343.
[39] F.H. Garner, R.B. Keey, Mass transfer from single solid spheres - II. Transfer in free convection, Chem. Eng. Sci. 9 (4) (1959) 218–224.
[40] A. Lochiel, P. Calderbank, Mass transfer in the continuous phase around axisymmetric bodies of revolution, Chem. Eng. Sci. 19 (7) (1964) 471–484.
[41] R.J. Good, L.A. Girifalco, A theory for estimation of surface and interfacial energies. III. Estimation of surface energies of solids from contact angle data, J. Phys. Chem. 64 (5) (1960) 561–565.
[42] J.N. Coupland, D.J. McClements, Physical properties of liquid edible oils, J. Am. Oil Chem. Soc. 74 (12) (1997) 1559–1564.
[43] P. Wang, A. Anderko, R.D. Young, Modeling viscosity of concentrated and mixed-solvent electrolyte systems, Fluid Phase Equil. 226 (1–2) (2004) 71–82.
[44] M. Negishi, H. Seto, M. Hase, K. Yoshikawa, How does the mobility of phospholipid molecules at a water/oil interface reflect the viscosity of the surrounding oil? Langmuir 24 (16) (2008) 8431–8434.
[45] A. Khopkar, A. Rammohan, V. Ranade, M. Dudukovic, Gas–liquid flow generated by a Rushton turbine in stirred vessel: CARPT/CT measurements and CFD simulations, Chem. Eng. Sci. 60 (2015) 2215–2229.
[46] F. Scargiali, A. Doorazio, F. Grisafi, A. Brucato, Modelling and simulation of gas–liquid hydrodynamics in mechanically stirred tanks, Chem. Eng. Res. Des. 85 (2007) 637–646.
[47] Y. Zhang, Y. Bai, H. Wang, CFD analysis of inter-phase forces in a bubble stirred vessel, Chem. Eng. Res. Des. 91 (2013) 29–35.
[48] T. Mahmud, J.N. Haque, K.J. Roberts, D. Rhodes, D. Wilkinson, Measurements and modelling of free-surface turbulent flows induced by a magnetic stirrer in an unbaffled stirred tank reactor, Chem. Eng. Sci. 64 (20) (2009) 4197–4209.
[49] M. Coroneo, G. Montante, A. Paglianti, F. Magelli, CFD predictions of fluid flow and mixing in stirred tanks: numerical issues about the RANS simulations, Comput. Chem. Eng. 35 (10) (2011) 1959–1968.
[50] S. Kresta, K. Bittorf, D. Wilson, Internal annular wall jets: radial flow in a stirred tank, AIChE J. 47 (11) (2001) 2390–2401.
[51] A. Ochieng, M.S. Onyango, A. Kumar, K. Kiriamiti, P. Musonge, Mixing in a tank stirred by a Rushton turbine at a low clearance, Chem. Eng. Process. Intensif. 47 (5) (2008) 842–851.
[52] Douglas E. Leng, Richard V. Calabrese, Immiscible liquid–liquid systems. Handbook of Industrial Mixing, Science and Practice, 2003, pp. 639–753.
[53] A.H. Skelland, R. Seksaria, Minimum impeller speeds for liquid-liquid dispersion in baffled vessels, Ind. Eng. Chem. Process Des. Dev. 17 (1) (1978) 55–61.